

KELT-14b AND KELT-15b: AN INDEPENDENT DISCOVERY OF WASP-122b AND A NEW HOT JUPITER

JOSEPH E. RODRIGUEZ¹, KNICOLE D. COLÓN^{2,3}, KEIVAN G. STASSUN^{1,4}, DUNCAN WRIGHT^{5,6}, PHILLIP A. CARGILE⁷, DANIEL BAYLISS⁸, JOSHUA PEPPER⁹, KAREN A. COLLINS¹, RUDOLF B. KUHN¹⁰, MICHAEL B. LUND¹, ROBERT J. SIVERD¹¹, GEORGE ZHOU^{7,12}, B. SCOTT GAUDI¹³, C.G. TINNEY^{5,6}, KALOYAN PENEV¹⁴, T.G. TAN¹⁵, CHRIS STOCKDALE^{16,17}, IVAN A. CURTIS¹⁸, DAVID JAMES¹⁹, STEPHANE UDRY⁸, DAMIEN SEGRANSAN⁸, ALLYSON BIERYLA⁷, DAVID W. LATHAM⁷, THOMAS G. BEATTY^{20,21}, JASON D. EASTMAN⁷, GORDON MYERS^{16,22}, JONATHAN BARTZ⁹, JOAO BENTO¹², ERIC L. N. JENSEN²³, THOMAS E. OBERST²⁴, DANIEL J. STEVENS¹³

¹Department of Physics and Astronomy, Vanderbilt University, 6301 Stevenson Center, Nashville, TN 37235, USA

²NASA Ames Research Center, M/S 244-30, Moffett Field, CA 94035, USA

³Bay Area Environmental Research Institute, 625 2nd St. Ste 209 Petaluma, CA 94952, USA

⁴Department of Physics, Fisk University, 1000 17th Avenue North, Nashville, TN 37208, USA

⁵School of Physics, UNSW Australia, 2052, Australia

⁶Australian Centre for Astrobiology, UNSW Australia, 2052, Australia

⁷Harvard-Smithsonian Center for Astrophysics, 60 Garden St, Cambridge, MA 02138, USA

⁸Observatoire Astronomique de l'Université de Genève, Chemin des Maillettes 51, 1290 Sauverny, Switzerland

⁹Department of Physics, Lehigh University, 16 Memorial Drive East, Bethlehem, PA 18015, USA

¹⁰South African Astronomical Observatory, PO Box 9, Observatory 7935, South Africa

¹¹Las Cumbres Observatory Global Telescope Network, 6740 Cortona Dr., Suite 102, Santa Barbara, CA 93117, USA

¹²Research School of Astronomy and Astrophysics, Australian National University, Canberra, ACT 2611, Australia

¹³Department of Astronomy, The Ohio State University, Columbus, OH 43210, USA

¹⁴Department of Astrophysical Sciences, Princeton University, Princeton, NJ 08544, USA

¹⁵Perth Exoplanet Survey Telescope, Perth, Australia

¹⁶American Association of Variable Star Observers, 49 Bay State Rd., Cambridge, MA 02138, USA

¹⁷Hazelwood Observatory

¹⁸Adelaide, Australia

¹⁹Cerro Tololo InterAmerican Observatory, Casilla 603, La Serena, Chile

²⁰Department of Astronomy & Astrophysics, The Pennsylvania State University, 525 Davey Lab, University Park, PA 16802

²¹Center for Exoplanets and Habitable Worlds, The Pennsylvania State University, 525 Davey Lab, University Park, PA 16802

²²5 Inverness Way, Hillsborough, CA 94010, USA

²³Department of Physics and Astronomy, Swarthmore College, Swarthmore, PA 19081, USA and

²⁴Department of Physics, Westminster College, New Wilmington, PA 16172, USA

Draft version November 15, 2018

ABSTRACT

We report the discovery of KELT-14b and KELT-15b, two hot Jupiters from the KELT-South survey. KELT-14b, an independent discovery of the recently announced WASP-122b, is an inflated Jupiter mass planet that orbits a $\sim 5.0^{+0.3}_{-0.7}$ Gyr, $V = 11.0$, G2 star that is near the main sequence turnoff. The host star, KELT-14 (TYC 7638-981-1), has an inferred mass $M_* = 1.18^{+0.05}_{-0.07} M_\odot$ and radius $R_* = 1.37 \pm 0.08 R_\odot$, and has $T_{\text{eff}} = 5802^{+95}_{-92}$ K, $\log g_* = 4.23^{+0.05}_{-0.04}$ and $[\text{Fe}/\text{H}] = 0.33 \pm 0.09$. The planet orbits with a period of 1.7100588 ± 0.0000025 days ($T_0 = 2457091.02863 \pm 0.00047$) and has a radius $R_p = 1.52^{+0.12}_{-0.11} R_J$ and mass $M_p = 1.196 \pm 0.072 M_J$, and the eccentricity is consistent with zero. KELT-15b is another inflated Jupiter mass planet that orbits a $\sim 4.6^{+0.5}_{-0.4}$ Gyr, $V = 11.2$, G0 star (TYC 8146-86-1) that is near the “blue hook” stage of evolution prior to the Hertzsprung gap, and has an inferred mass $M_* = 1.181^{+0.051}_{-0.050} M_\odot$ and radius $R_* = 1.48^{+0.09}_{-0.04} R_\odot$, and $T_{\text{eff}} = 6003^{+56}_{-52}$ K, $\log g_* = 4.17^{+0.02}_{-0.04}$ and $[\text{Fe}/\text{H}] = 0.05 \pm 0.03$. The planet orbits on a period of 3.329441 ± 0.000016 days ($T_0 = 2457029.1663 \pm 0.0073$) and has a radius $R_p = 1.443^{+0.11}_{-0.057} R_J$ and mass $M_p = 0.91^{+0.21}_{-0.22} M_J$ and an eccentricity consistent with zero. KELT-14b has the second largest expected emission signal in the K-band for known transiting planets brighter than $K < 10.5$. Both KELT-14b and KELT-15b are predicted to have large enough emission signals that their secondary eclipses should be detectable using ground-based observatories.

Subject headings: planetary systems, stars: individual: KELT-14, stars: individual: KELT-15, techniques: photometric, techniques: radial velocities, techniques: spectroscopic

1. INTRODUCTION

The confirmation of over 1000 transiting exoplanets to date is due to the success of ground-based photometric surveys such as HATNet (Bakos et al. 2004), SuperWASP (Pollacco et al. 2006), XO (McCullough et al. 2006), and TrES (Alonso et al. 2004), and the space-based missions CoRoT (Baglin et al. 2006) and Kepler (Borucki et al. 2010). The field has shifted from pure discovery to understanding the demographics of exoplanets and atmospheric characteri-

zation. However, many of the discovered planets are too faint or too small for performing atmospheric characterization with current facilities. To date, there are only 29 giant transiting planets orbiting stars with $V < 11.5$ in the southern hemisphere¹.

It is believed that “hot Jupiters,” gas giant planets that orbit extremely close (orbital periods of a few days) to their host stars, must form beyond the

¹ www.exoplanets.org, as of September 2015

“Snow Line.” Once formed, the giant planets can migrate inward through various methods (Tanaka et al. 2002; Masset & Papaloizou 2003; D’Angelo & Lubow 2008; Jackson et al. 2008; Cloutier & Lin 2013). It has been proposed that Jupiter experienced migration early in its lifetime, but did not migrate all the way inward due to the gravitational pull of Saturn (Walsh et al. 2011). These hot Jupiters, specifically ones orbiting solar-like stars, provide insight into alternate evolutionary scenarios.

The Kilodegree Extremely Little Telescope (KELT) exoplanet survey, operated and owned by Vanderbilt University, Ohio State University, and Lehigh University, has been observing $> 60\%$ of the sky with a cadence of 10 to 20 minutes for many years. The project uses two telescopes, KELT-North at Winer Observatory in Sonoita, Arizona and KELT-South at the South African Astronomical Observatory (SAAO) in Sutherland, South Africa. The survey is optimized for high-precision ($\leq 1\%$) photometry for stars with $8 \leq V \leq 11$ to enable transit discovery of giant planets. Each telescope has a 42 mm aperture, $26^\circ \times 26^\circ$ field of view, and a pixel scale of $23''/\text{pixel}$ (Pepper et al. 2007, 2012). The first telescope in the survey, KELT-North, has announced six planets orbiting stars brighter than $V = 11$ (Siverv et al. 2012; Beatty et al. 2012; Pepper et al. 2013; Collins et al. 2014; Bieryla et al. 2015; Fulton et al. 2015). The younger counterpart in the survey, KELT-South, has already announced one planet, KELT-10b (Kuhn et al. 2015).

In this paper, we present the discovery of a new hot Jupiter by KELT-South, which we name KELT-15b. We also present another hot Jupiter, which we refer to in this paper as KELT-14b. Shortly before the completion of this paper, a draft manuscript was posted to the arXiv (Turner et al. 2015) describing the discovery of three new exoplanets by the Super-WASP survey. One of the planets they name WASP-122b, which is the same planet we designate as KELT-14b. Since the data we present in this paper were collected independently and the analysis performed before the announcement of WASP-122b, we have chosen to discuss our findings as an independent discovery of this planet, and we refer to it here as KELT-14b. However, we acknowledge the prior announcement of it as WASP-122b.

2. DISCOVERY AND FOLLOW-UP OBSERVATIONS

2.1. KELT-South

KELT-14 and KELT-15 are located in the KELT-South field 34, which is centered at J2000 $\alpha = 08^h 16^m 12^s$ $\delta = -54^\circ 00' 00''$. Field 34 was monitored in two separate campaigns: First from UT 2010 January 03 to UT 2010 February 19 as part of the KELT-South commissioning campaign, and then again from UT 2012 September 16 to UT 2014 June 14, acquiring a total of ~ 5780 images after post-processing and removal of bad images. Following the strategy described in Kuhn et al. (2015), we reduced the raw images, extracted the light curves, and searched for transit candidates. Two stars emerged as top candidates from this process: KS34C030815 (TYC 7638-981-1, GSC 07638-00981, 2MASS J07131235-4224350) located at $\alpha = 07^h 13^m 12^s.347$ $\delta = -42^\circ 24' 35''.17$ J2000, hereafter as KELT-14, and KS34C034621 (TYC 8146-86-1, GSC 08146-00086, 2MASS J07493960-5207136) located at $\alpha = 07^h 49^m 39^s.606$ $\delta = -52^\circ 07' 13''.58$ J2000, designated as KELT-15 (see Figure 1). The host star properties for both targets are listed in Table 1. We used the box-fitting least squares (BLS) algorithm (Kovács et al. 2002; Hartman 2012) to select

these candidates, and the BLS selection criteria and values for both are shown in Table 2.

2.2. Photometric Follow-up

To precisely measure the transits of KELT-14b and KELT-15b, we obtained high-cadence, high-precision photometric follow-up using larger telescopes that cleanly resolve the hosts from their neighbors. These observations better constrain the period, depth, and duration of the transit and also rule out various false positive scenarios. To predict the transits, we use the web interface, TAPIR (Jensen 2013). For consistency, all follow-up observations were analyzed using AstroImageJ (AIJ) (Collins & Kielkopf 2013; Collins 2015). This software also provides the best detrending parameters that are included in the global fit (see §4.1). The follow-up photometry for KELT-14b and KELT-15b are shown in Figures 2 and 3 respectively.

2.2.1. LCOGT

We observed a nearly full transit of KELT-14b in the Sloan g -band on UT 2015 March 29 from a 1-m telescope in the Las Cumbres Observatory Global Telescope (LCOGT) network² located at Cerro Tololo Inter-American Observatory (CTIO) in Chile. The LCOGT telescopes at CTIO have a $4K \times 4K$ Sinistro detector with a $27' \times 27'$ field of view and a pixel scale of $0.39''$ per pixel. The reduced data were downloaded from the LCOGT archive and analyzed using the AstroImageJ software. In a portion of the light curve surrounding the transit ingress the target was saturated, therefore we exclude this data from the global parameter analysis in §4.1.

2.2.2. PEST Observatory

PEST (Perth Exoplanet Survey Telescope) observatory is a home observatory owned and operated by Thiam-Guan (TG) Tan. It is equipped with a 12-inch Meade LX200 SCT $f/10$ telescope with focal reducer yielding $f/5$. The camera is an SBIG ST-8XME, and focusing is computer controlled with an Optec TCF-Si focuser. PEST observed a full transit of KELT-14b on UT 2015 January 20 (R), UT 2015 January 25 (I) and UT 2015 March 09 (V). PEST observed a full transit of KELT-15b on UT 2015 January 16 (I).

2.2.3. Hazelwood Observatory

The Hazelwood Observatory, operated by Chris Stockdale in Victoria, Australia, obtained an ingress of KELT-14b in V -band on UT 2015 March 09, a full transit in the B -band on UT 2015 March 21 and a full transit in I -band on UT 2015 April 02. The observatory uses a 0.32-m Planewave CDK telescope with a SBIG ST8XME 1.5K x 1K CCD, giving a $18' \times 12'$ field of view, and has a pixel scale of $0.73''$ per pixel.

2.2.4. Adelaide Observations

The Adelaide Observatory, owned and operated by Ivan Curtis is located in Adelaide, Australia (labeled “ICO” in the figures). The observatory is equipped with a 9.25-in Celestron SCT telescope with an Antares 0.63 \times focal reducer yielding an overall focal ratio of $f/6.3$. The camera is an Atik 320e, which uses a cooled Sony ICX274 CCD of 1620×1220 pixels. The field of view is $16.6' \times 12.3'$ with a pixel scale of $0.62''$ per pixel. The Adelaide Observatory observed a full transit of KELT-14b on UT 2015 March 09 (V) and full transits of KELT-15b on UT 2014 December 27 (R) and UT 2015 January 06 (R).

² <http://lco.net/>

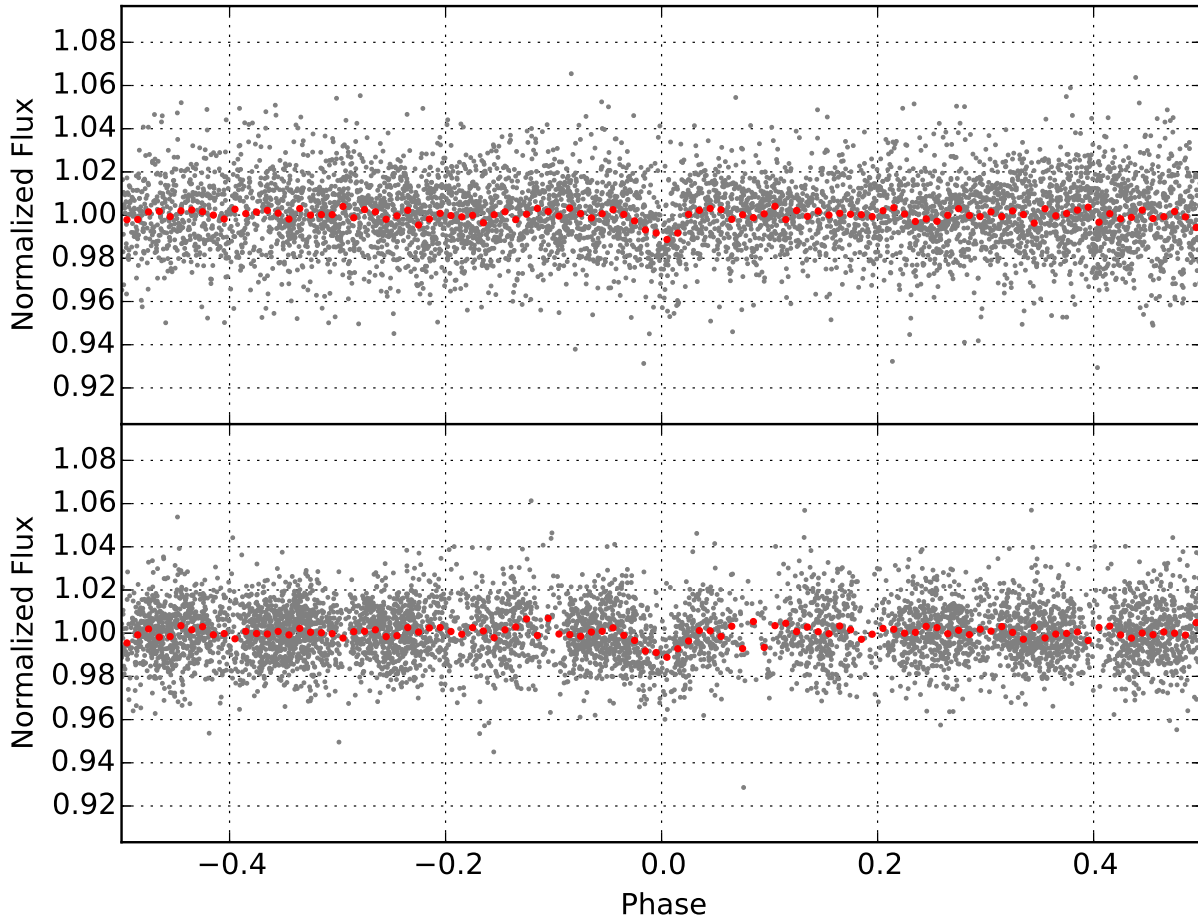


FIG. 1.— Discovery light curve of KELT-14b (Top) and KELT-15b (Bottom) from the KELT-South telescope. The light curves are phase-folded to the discovery periods of $P = 1.7100596$ and 3.329442 days respectively; the red points show the light curve binned in phase using a bin size of 0.01.

2.3. Spectroscopic Follow-up

2.3.1. Reconnaissance Spectroscopy

Since many astrophysical phenomena can create photometric signals that mimic planetary transits, it is important to follow up all candidates carefully to eliminate false positives. After identifying the targets as planet candidates from the KELT photometry, a first stage of spectroscopic reconnaissance was done using the WiFeS spectrograph mounted on the 2.3m ANU telescope at Siding Spring Observatory (Dopita et al. 2007). This instrument is an optical dual-beam, image-slicing integral-field spectrograph. The full WiFeS observing strategy and reduction procedure is described in Bayliss et al. (2013).

First, observations of both stars were performed at low resolution ($R \sim 3000$) in the 3500-6000 Å range to determine their stellar type. Both KELT-14 and KELT-15 were identified with the following parameters: KELT-14 has $T_{\text{eff}} = 5572 \pm 200\text{K}$, $\log g_* = 3.5 \pm 0.4$ (cgs) and $[\text{Fe}/\text{H}] = 0.0 \pm 0.4$; KELT-15b has $T_{\text{eff}} = 6221 \pm 200\text{K}$, $\log g_* = 3.4 \pm 0.4$ (cgs) and $[\text{Fe}/\text{H}] = 0.0 \pm 0.4$. The low resolution spectra provide poor precision on the $\log g_*$ and therefore, these $\log g_*$ values aren't very reliable.

Additionally, three observations for each target were performed in medium-resolution ($R \sim 7000$) using the red camera arm of the WiFeS spectrograph (5500-9000 Å) across the expected orbital phase based on the photometrically detected

period. These observations were aimed at performing multiple radial velocity (RV) measurements of each target to detect signals higher than 5 km/s amplitude, allowing us to identify grazing binary systems or blended eclipsing binaries. The typical RV precision achieved with this instrument is around 1.5 km/s, and both targets showed no significant variations among the three measurements.

2.3.2. High Precision Spectroscopic Follow-up

To confirm the planetary nature of the companion, we obtain multi-epoch high-resolution spectroscopy. These spectra allow us to very accurately measure the radial velocity of the host star providing us with a precise measurement of the companion's mass. Also, these spectra provide a much better estimate of the stellar properties.

2.3.3. CYCLOPS2

Spectroscopic observations of KELT-14 and KELT-15 were carried out using the CYCLOPS2 illuminating the UCLES spectrograph instrument on the Anglo-Australian Telescope (AAT) over two observing runs: UT 2015 February 02 - UT 2015 March 01 and UT 2015 May 6 - UT 2015 May 13 (See Figure 4 and 5). The instrumental set-up and observing strategy for these observations closely follow that described in earlier CYCLOPS radial velocity papers (Addison et al. 2013, 2014).

CYCLOPS2 is a Cassegrain fiber-based integral field unit which reformats a $\sim 2.5''$ diameter on-sky aperture into a

TABLE 1
STELLAR PROPERTIES OF KELT-14 AND KELT-15 OBTAINED FROM THE LITERATURE.

Parameter	Description	KELT-14 Value	KELT-15 Value	Source	Reference(s)
		TYC 7638-981-1	TYC 8146-86-1		
		GSC 07638-00981	GSC 08146-00086		
		2MASS J07131235-4224350	2MASS J07493960-5207136		
α_{J2000}	Right Ascension (RA)	07:13:12.347	07:49:39.606	Tycho-2	Høg et al. (2000)
δ_{J2000}	Declination (Dec)	-42:24:35.17	-52:07:13.58	Tycho-2	Høg et al. (2000)
NUV		17.06± 0.1	N/A	GALEX	
B_T	Tycho B_T magnitude	11.963	11.889	Tycho-2	Høg et al. (2000)
V_T	Tycho V_T magnitude	11.088	11.440	Tycho-2	Høg et al. (2000)
Johnson V	APASS magnitude	10.948 ± 0.05	11.189± 0.05	APASS	et al. (2015)
Johnson B	APASS magnitude	11.64 ± 0.05	11.745± 0.05	APASS	et al. (2015)
Sloan g'	APASS magnitude	11.247 ± 0.051	11.438 ± 0.03	APASS	et al. (2015)
Sloan r'	APASS magnitude	10.733 ± 0.053	11.048 ± 0.03	APASS	et al. (2015)
Sloan i'	APASS magnitude	10.631 ± 0.05	10.935 ± 0.05	APASS	et al. (2015)
J	2MASS magnitude	9.808 ± 0.024	10.205 ± 0.024	2MASS	Cutri et al. (2003)
H	2MASS magnitude	9.487 ± 0.024	9.919 ± 0.023	2MASS	Cutri et al. (2003)
K	2MASS magnitude	9.424 ± 0.023	9.854 ± 0.025	2MASS	Cutri et al. (2003)
WISE1	WISE passband	9.369 ± 0.023	9.775 ± 0.023	WISE	Cutri & et al. (2012)
WISE2	WISE passband	9.414 ± 0.021	9.805 ± 0.020	WISE	Cutri & et al. (2012)
WISE3	WISE passband	9.339 ± 0.026	9.919 ± 0.048	WISE	Cutri & et al. (2012)
WISE4	WISE passband	9.442 ± 0.495	<9.580	WISE	Cutri & et al. (2012)
μ_α	Proper Motion in RA (mas yr ⁻¹)	-13.9 ± 2.2	-3.4 ± 2.3	NOMAD	Zacharias et al. (2004)
μ_δ	Proper Motion in DEC (mas yr ⁻¹)	-1.3 ± 2.0	-2.0 ± 2.9	NOMAD	Zacharias et al. (2004)
U*	Space motion (km s ⁻¹)	-4.6 ± 1.9	7.8 ± 3.8		This work
V	Space motion (km s ⁻¹)	-14.6 ± 0.9	2.6 ± 0.8		This work
W	Space motion (km s ⁻¹)	-14.0 ± 2.3	-1.5 ± 3.3		This work
Distance	Estimated Distance (pc)	201±19	291±30		This work
RV	Absolute RV (km s ⁻¹)	34.62 ± 0.13	12.20 ± 0.11		This work

NOTES

Red value correspond to upper limits ($S/N < 2$)
*U is positive in the direction of the Galactic Center

TABLE 2
KELT-SOUTH BLS SELECTION CRITERIA

BLS Statistic	Selection Criteria	KELT-14b KS34C030815	KELT-15b KS34C034621
Signal detection efficiency	SDE > 7.0	7.75403	11.04677
Signal to pink-noise	SPN > 7.0	8.26194	9.78164
Transit depth	$\delta < 0.05$	0.01072	0.00841
χ^2 ratio	$\frac{\Delta\chi^2}{\Delta\chi^2_-} > 1.5$	2.16	2.56
Duty cycle	$q < 0.1$	0.03333	0.04667

pseudo-slit of dimensions equivalent to 0.6'' wide \times 14.5'' long (Horton et al. 2012). CYCLOPS2 has 16 on-sky fibers, plus one fiber illuminated by a ThUXe lamp. Each fiber delivers a spectral resolution of $\lambda/\Delta\lambda \approx 70,000$ over 19 echelle orders in the wavelength range of 4550 – 7350Å, when used with the UCLES spectrograph in its 79 line/mm grating configuration.

We use a ThAr calibration lamp to illuminate all of the on-sky fibers at the beginning of observations to create a *reference* ThAr wavelength solution. We then use simultaneous ThUXe data from each exposure to determine low-order distortions which differentially calibrate observations through

the night onto the *reference* ThAr solution. These reductions are carried out using custom MATLAB routines (Wright and Tinney, *in prep.*). Calibration precision is estimated from the scatter of fits to the simultaneous ThUXe spectral features and these are tested against velocity standards taken each night. The typical calibration precision is $< 10 \text{ m s}^{-1}$. This calibration error is combined with the error from a fit to the cross-correlation profile to give a final uncertainty for each observation.

The cross-correlation profiles are obtained using a weighted cross-correlation (Baranne et al. 1996; Pepe et al. 2002) of a stellar template produced with SYNPEC (Hubeny & Lanz 2011). The velocities are determined from the fit of a generalised normal distribution to the cross-correlation profiles and the errors are estimated from the Jacobian matrix for each fit. We find no correlation between the bisector spans and the measured radial velocities. This provides strong evidence against a blended eclipsing binary scenario.

2.3.4. CORALIE

CORALIE is a fibre-fed echelle spectrograph (Queloz et al. 2001) attached to the Swiss 1.2 m Leonard Euler telescope at the ESO La Silla Observatory in Chile. It has a spectral resolution of $R \sim 60000$, and is able to measure radial velocities of bright stars to a precision of 3 m.s^{-1} or better

TABLE 3
PHOTOMETRIC FOLLOW-UP OBSERVATIONS AND THE DETRENDING PARAMETERS FOUND BY AIJ FOR THE GLOBAL FIT.

Target	Follow-up Observer	Date (UT)	Filter	Detrending parameters used in the global fit
KELT-14b	PEST	UT 2015 January 20	<i>R</i>	airmass, y coordinates
KELT-14b	PEST	UT 2015 January 25	<i>I</i>	airmass, y coordinates
KELT-14b	PEST	UT 2015 March 09	<i>V</i>	airmass
KELT-14b	Adelaide	UT 2015 March 09	<i>V</i>	airmass, total counts
KELT-14b	Hazelwood	UT 2015 March 09	<i>V</i>	airmass
KELT-14b	Hazelwood	UT 2015 March 21	<i>B</i>	airmass
KELT-14b	LCOGT	UT 2015 March 29	<i>g'</i>	airmass, pixel width, total counts
KELT-14b	Hazelwood	UT 2015 April 02	<i>I</i>	airmass
KELT-15b	Adelaide	UT 2014 December 27	<i>V</i>	airmass, y coordinates, total counts
KELT-15b	Adelaide	UT 2015 January 06	<i>R</i>	airmass, y coordinates
KELT-15b	PEST	UT 2015 January 16	<i>I</i>	airmass, sky counts per pixel, total counts

NOTES

All the follow-up photometry presented in this paper is available in machine-readable form in the online journal.

TABLE 4
KELT-14 RADIAL VELOCITY OBSERVATIONS WITH CYCLOPS2.

BJD _{TDB}	RV (m s ⁻¹)	RV error (m s ⁻¹)	Instrument
2457083.075531623	34431.30	6.00	CYCLOPS2
2457148.892669835	34776.70	9.80	CYCLOPS2
2457148.924568460	34792.00	12.60	CYCLOPS2
2457149.929456027	34505.50	19.10	CYCLOPS2
2457150.967262368	34528.10	13.10	CYCLOPS2
2457151.873724511	34733.40	14.30	CYCLOPS2
2457153.886260897	34794.20	13.20	CYCLOPS2
2457153.916879608	34729.70	14.90	CYCLOPS2
2457154.898109197	34468.40	8.30	CYCLOPS2
2457155.867229521	34533.50	112.90	CYCLOPS2
2457155.900058155	34560.60	111.50	CYCLOPS2
2457079.939623842	34621.30	16.70	CYCLOPS2
2457079.991772522	34658.60	8.20	CYCLOPS2
2457080.950428010	34456.10	5.20	CYCLOPS2
2457081.937382183	34725.20	5.50	CYCLOPS2

NOTES

This table is available in its entirety in a machine-readable form in the online journal.

(Pepe et al. 2002). In June 2015, the CORALIE spectrograph was equipped with a new Fabry-Pérot-based calibration system (Wildi et al. 2011). This system replaces the ThAr lamp for the simultaneous reference method that determines and corrects for instrumental drift occurring between the calibration and the science exposure (Baranne et al. 1996). The data-reduction software has been adapted to take into account the new operational mode and take benefit from the higher spectral content, and hence the lower photon noise, on the drift measurement, provided by the Fabry-Pérot based calibration source. We obtained spectra at five epochs of KELT-15 from UT 2015 September 02 to UT 2015 September 14. All observations were reduced and radial velocities were computed in real time using the standard CORALIE pipeline. The observations from CORALIE are consistent with the CYCLOPS2 measured radial velocities. The results are shown in Figure 5. We find no correlation between the bisector spans and the measured radial velocities (see Figure 6).

3. ANALYSIS AND RESULTS

3.1. *SME* Stellar Analysis

TABLE 5
KELT-15 RADIAL VELOCITY OBSERVATIONS WITH CYCLOPS2 AND CORALIE.

BJD _{TDB}	RV (m s ⁻¹)	RV error (m s ⁻¹)	Instrument
2457083.091453823	12105.7	17.6	CYCLOPS2
2457148.910598987	12074.4	16.3	CYCLOPS2
2457148.942507928	12247.1	16.6	CYCLOPS2
2457149.947425124	12072.9	25.1	CYCLOPS2
2457150.985251112	12191.4	17.6	CYCLOPS2
2457151.891071429	12281.0	15.0	CYCLOPS2
2457151.953179348	12291.2	12.7	CYCLOPS2
2457153.903635089	12196.2	16.0	CYCLOPS2
2457153.934254059	12188.1	19.9	CYCLOPS2
2457154.912681718	12334.9	13.3	CYCLOPS2
2457154.921681414	12354.9	17.5	CYCLOPS2
2457155.886209486	12085.3	118.0	CYCLOPS2
2457155.918108410	12057.5	114.8	CYCLOPS2
2457081.094367965	12320.4	10.8	CYCLOPS2
2457269.908610	12096.39	53.81	CORALIE
2457272.903199	12125.96	81.47	CORALIE
2457273.907330	12221.40	57.97	CORALIE
2457276.897042	12216.76	44.60	CORALIE
2457278.894140	12161.43	24.16	CORALIE

NOTES

This table is available in its entirety in a machine-readable form in the online journal.

In order to determine precise stellar parameters for KELT-14 and KELT-15, we use the available high-resolution, low S/N AAT CYCLOPS2 spectra acquired for radial velocity confirmation of the two planetary systems. For each CYCLOPS2 dataset, we took the flux weighted mean of the individual fibers, continuum normalized each spectral order, and stitched the orders into a single 1-D spectrum. We shifted each resulting spectrum to rest wavelength by accounting for barycentric motion, and median combined all observations into a single spectrum with a S/N ~ 50 , sufficient for detailed spectroscopic analysis.

Stellar parameters for KELT-14 and KELT-15 are determined using an implementation of Spectroscopy Made Easy (SME) (Valenti & Piskunov 1996). Our Monte Carlo approach to using SME for measuring stellar parameters is detailed in Kuhn et al. (2015). Briefly, we use a multi-trial minimization of 500 randomly selected initial parameter values, each solving for 5 free parameters: effective tempera-

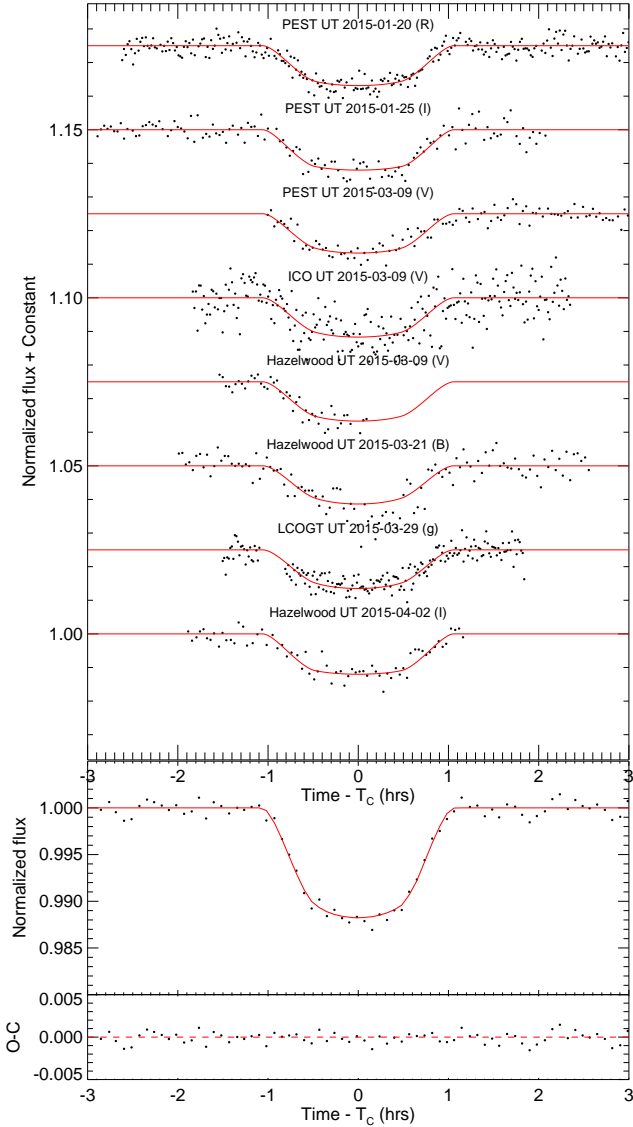


FIG. 2.— (Top) The follow-up photometry of KELT-14b from the KELT follow-up network. The red line is the best model for each follow-up lightcurve. (Bottom) The individual follow-up lightcurves combined and binned in 5 minute intervals. This combined and binned plot represents the true nature of the transit. The combined and binned light curve is for display and is not used in the analysis. The red line represents the combined and binned individual models (red) of each follow-up observation.

ture (T_{eff}), surface gravity ($\log g_*$), iron abundance ($[\text{Fe}/\text{H}]$), metal abundance ($[\text{M}/\text{H}]$), and rotational velocity of the star ($v \sin I_*$). We determine our final measured stellar properties by identifying the output parameters that give the optimal SME solution (i.e., the solution with the lowest χ^2). The overall SME measurement uncertainties in the final parameters are calculated by adding in quadrature the internal error determined from the 68.3% confidence region in the χ^2 map, the median absolute deviation of the parameters from the 500 output SME solutions to account for the correlation between the initial guess and the final fit, and an estimate for the systematic errors in our method when compared to other common stellar spectral analysis tools (see Gómez Maqueo Chew et al. 2013).

Due to the instrument setup used for measuring high-precision radial velocities, the AAT CYCLOPS2 spectra do

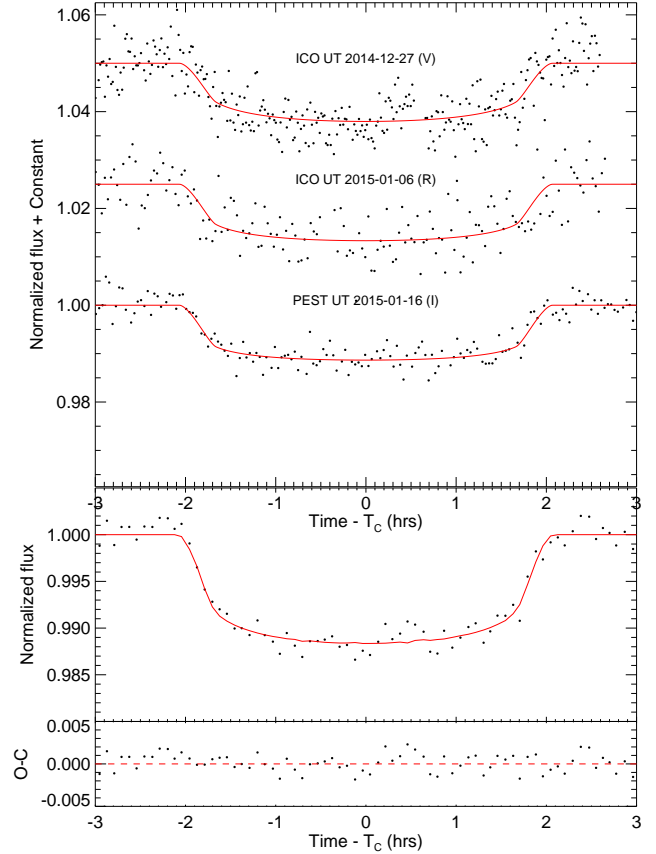


FIG. 3.— (Top) The follow-up photometry of KELT-15b from the KELT follow-up network. The red line is the best model for each follow-up lightcurve. (Bottom) All the follow-up lightcurves combined and binned in 5 minute intervals. This best represents the true nature of the transit. The combined and binned light curve is for display and is not used in the analysis. The red line represents the combined and binned individual models (red) of each follow-up observation.

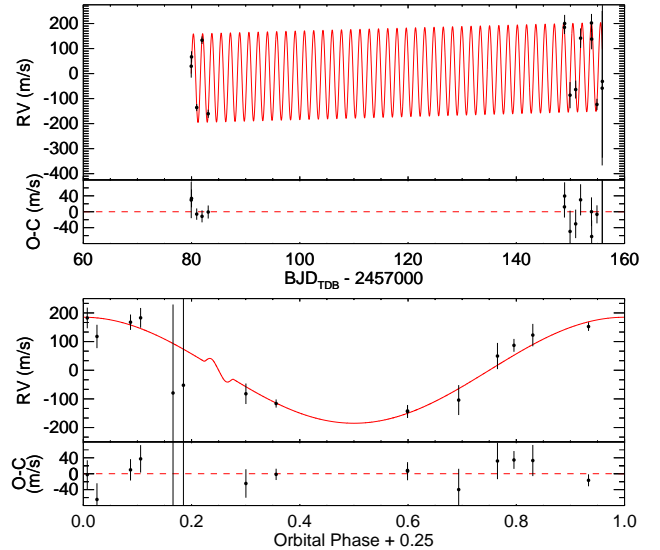


FIG. 4.— (Top) the AAT radial velocity measurements (the median absolute RV has been subtracted off) and residuals for KELT-14. The best-fitting orbit model is shown in red. The residuals of the RV measurements to the best fitting model are shown below. (Bottom) The KELT-14 AAT measurements phase-folded to the final global fit ephemeris.

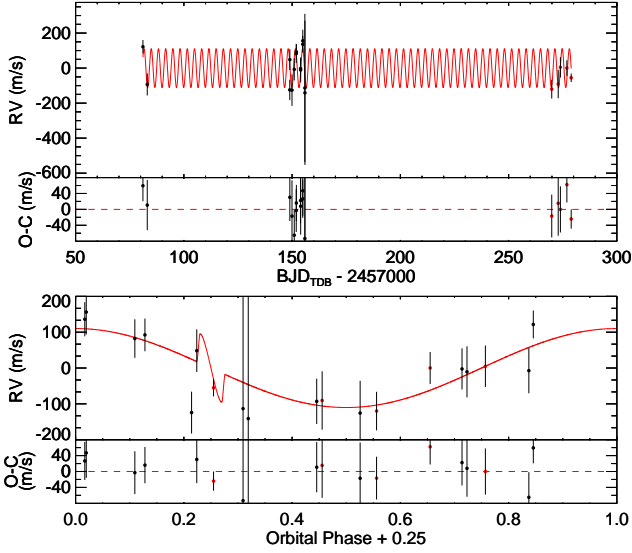


FIG. 5.— (Top) the AAT (black) and CORALIE (red) radial velocity measurements (the median absolute RV has been subtracted off) and residuals for KELT-15. The best-fitting orbit model is shown in red. The residuals of the RV measurements to the best model are shown below. (Bottom) The KELT-15 AAT (black) and CORALIE (red) measurements phase-folded to the final global fit ephemeris.

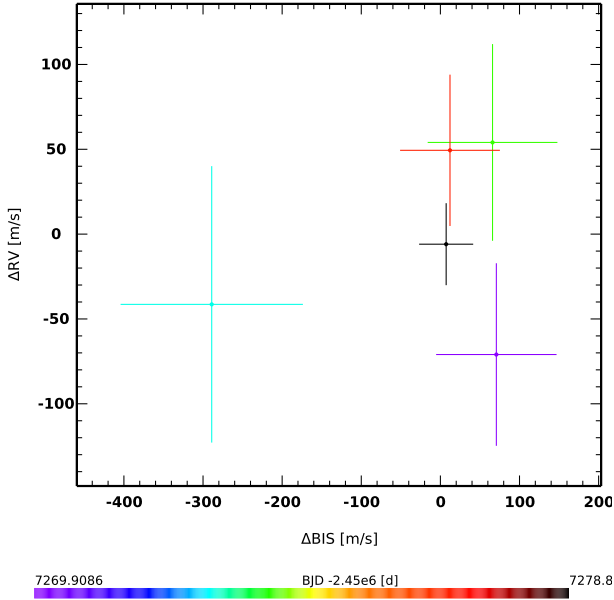


FIG. 6.— The CORALIE Bisector measurements for the KELT-15 spectra used for radial velocity measurements. We find no significant correlation between RV and the bisector spans.

not include the full MgB triplet wavelength region, a pressure-broadened set of lines commonly used in spectral synthesis modeling to constrain $\log g_*$ (Valenti & Fischer 2005). The available spectra only include one of the three strong Mg lines in this region. In order to investigate the effect of this constraint on our stellar parameters, we run two separate SME runs for both KELT-14 and KELT-15, one with $\log g_*$ as a free parameter and the other with $\log g_*$ fixed from our preliminary global fit of the photometric observations.

Our final SME spectroscopic parameters for KELT-14 are: $T_{\text{eff}} = 5817 \pm 90$ K, $\log g_* = 4.16 \pm 0.12$, $[\text{m}/\text{H}] = 0.39 \pm 0.03$, $[\text{Fe}/\text{H}] = 0.34 \pm 0.09$ and a projected rotational velocity

$v \sin I_* = 7.7 \pm 0.4$ km s $^{-1}$. Similarly, with a fixed $\log g_* = 4.23$; $T_{\text{eff}} = 5834 \pm 75$ K, $[\text{m}/\text{H}] = 0.39 \pm 0.03$, $[\text{Fe}/\text{H}] = 0.34 \pm 0.09$ and $v \sin I_* = 7.6 \pm 0.4$ km s $^{-1}$. For KELT-15 we find: $T_{\text{eff}} = 6023 \pm 61$ K, $\log g_* = 3.80 \pm 0.08$, $[\text{m}/\text{H}] = 0.06 \pm 0.03$, $[\text{Fe}/\text{H}] = 0.05 \pm 0.03$ and $v \sin I_* = 11.1 \pm 0.5$ km s $^{-1}$. With a fixed $\log g_* = 4.17$ we find; $T_{\text{eff}} = 6102 \pm 51$ K, $[\text{m}/\text{H}] = 0.02 \pm 0.03$, $[\text{Fe}/\text{H}] = 0.05 \pm 0.03$ and $v \sin I_* = 11.1 \pm 0.5$ km s $^{-1}$. We constrain the macro- and microturbulent velocities to the empirically constrained relationship (Gómez Maqueo Chew et al. 2013). However, we do allow them to change during our modelling according to the other stellar parameters. Our best fitting stellar parameters result in $v_{\text{mac}} = 4.05$ km s $^{-1}$ and $v_{\text{mic}} = 1.00$ km s $^{-1}$ for KELT-14, and for KELT-15 $v_{\text{mac}} = 4.37$ km s $^{-1}$ and $v_{\text{mic}} = 1.19$ km s $^{-1}$.

3.2. SED Analysis

We construct empirical spectral energy distributions (SEDs) of KELT-14 and KELT-15 using all available broad-band photometry in the literature, shown in Figure 7. We use the near-UV flux from GALEX (Martin et al. 2005), the B_T and V_T fluxes from the Tycho-2 catalogue, B , V , g' , r' , and i' fluxes from the AAVSO APASS catalogue, NIR fluxes in the J , H , and K_S bands from the 2MASS Point Source Catalogue (Cutri et al. 2003; Skrutskie et al. 2006), and near- and mid-infrared fluxes in the WISE passbands (Wright et al. 2010).

We fit these fluxes using the Kurucz atmosphere models (Castelli & Kurucz 2004) by fixing the values of T_{eff} , $\log g_*$ and $[\text{Fe}/\text{H}]$ inferred from the global fit to the lightcurve and RV data as described in §4.1 and listed in Table 4 and Table 5, and then finding the values of the visual extinction A_V and distance d that minimize χ^2 , with a maximum permitted A_V based on the full line-of-sight extinction from the dust maps of Schlegel et al. (1998) (maximum $A_V = 0.50$ mag and 0.89 mag for KELT-14 and KELT-15, respectively).

For KELT-14 we find $A_V = 0.1 \pm 0.1$ mag and $d = 201 \pm 19$ pc with the best fit model having a reduced $\chi^2 = 1.39$. For KELT-15 we find $A_V = 0.18 \pm 0.12$ and $d = 291 \pm 30$ pc with the best fit model having a reduced $\chi^2 = 0.84$. This implies a very good quality of fit and further corroborates the final derived stellar parameters for the KELT-14 and KELT-15 host stars. We note that the quoted statistical uncertainties on A_V and d are likely to be underestimated because alternate model atmospheres would predict somewhat different SEDs and thus values of extinction and distance, but for stars of the masses and temperatures of KELT-14 and KELT-15 the systematic differences among various model atmospheres are not expected to be large.

3.3. Evolutionary State

To better place the KELT-14 and KELT-15 systems in context, we show in Figure 8 the H-R diagrams for the two systems in the T_{eff} versus $\log g_*$ plane. In each case, we use the Yonsei-Yale stellar evolution model track (Demarque et al. 2004) for a star with the mass and metallicity inferred from the final global fit (this fit used the SME determined $[\text{Fe}/\text{H}]$ and T_{eff} , where $\log g_*$ was not fixed, as priors), where the shaded region represents the mass and $[\text{Fe}/\text{H}]$ fit uncertainties. The model isochrone ages are indicated as blue points, and the final best global fit T_{eff} and $\log g_*$ values are represented by the red error bars. For comparison, the T_{eff} and $\log g_*$ values determined from spectroscopy alone with $\log g_*$ not fixed are represented by the green error bars while the

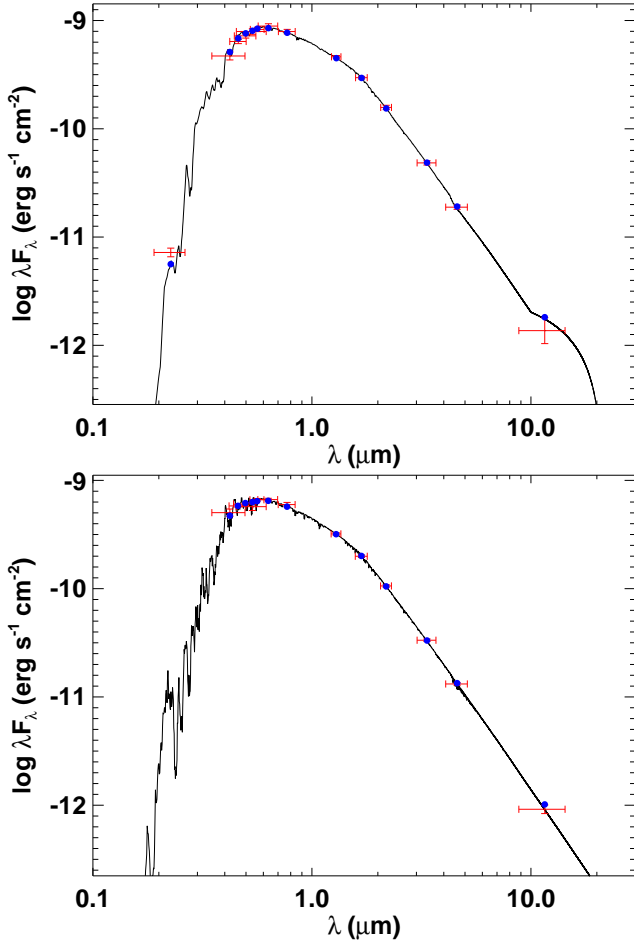


FIG. 7.— The SED fit for (top) KELT-14 and (bottom) KELT-15. The red points show the photometric values and errors given in Table 1. The blue points are the predicted integrated fluxes at the corresponding bandpass. The black line represents the best fit stellar atmospheric model.

blue error bars represent when the $\log g_*$ was fixed in the SME analysis (Figure 8).

KELT-14 is a G2 type star near the main-sequence turnoff but not yet in the Hertzsprung gap, with an age of $\sim 5.0^{+0.3}_{-0.7}$ Gyr. KELT-15 is a G0 type star with an age of $\sim 4.6^{+0.5}_{-0.4}$ Gyr, on or near the “blue hook” just prior to the Hertzsprung gap. These classifications are also consistent with those reported in the catalogs of Pickles & Depagne (2010) and Ammons et al. (2006).

3.4. UVW Space motion

To better understand the place of KELT-14 and KELT-15 in the galaxy, we calculate the UVW space motion. This exercise can allow us to determine the membership and possibly the age of a star if it is associated with any known stellar groups. To calculate the UVW space motion, we combine the information presented in Table 1 with the determined distance to KELT-14 and KELT-15 from the SED analysis (201 ± 19 pc and 291 ± 30 pc respectively). We also estimated the absolute radial velocity and error by taking the average and standard deviation of all the measured radial velocities by AAT. This gave us an estimated absolute radial velocity of 34.62 ± 0.13 km s^{-1} and 12.20 ± 0.11 m s^{-1} for KELT-14b and KELT-15b, respectively. We calculate the space motion to be $U = -4.6 \pm 1.9$ km s^{-1} , $V = -14.6 \pm 0.9$ km s^{-1} , $W = -14.0 \pm$

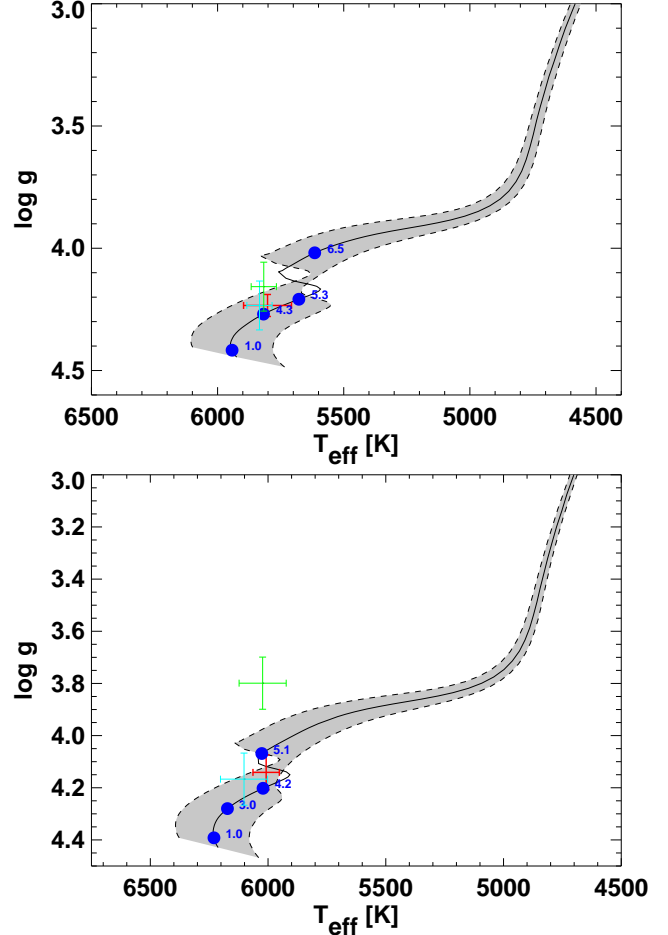


FIG. 8.— The theoretical H-R diagrams for (top) KELT-14 and (bottom) KELT-15 using the Yonsei-Yale stellar evolution models (Demarque et al. 2004). The $\log g_*$ values are in cgs units. The red cross represents the values from the final global fit. The blue cross is the position and errors of the SME analysis when $\log g_*$ was fixed at the initial global fit value and the green cross is when $\log g_*$ was not fixed. The dashed lines at the edge of the gray shaded region represent the 1σ uncertainties on M_* and $[\text{Fe}/\text{H}]$ from the global fit. The various ages along the tracks are represented by the blue points.

2.3 km s^{-1} for KELT-14 and $U = 7.8 \pm 3.8$ km s^{-1} , $V = 2.6 \pm 0.8$ km s^{-1} , $W = -1.5 \pm 3.3$ km s^{-1} for KELT-15 (positive U pointing toward the Galactic center). These space motion values give a 99% chance that both KELT-14 and KELT-15 belong to the thin disk, according to the classification scheme of Bensby et al. (2003)

4. PLANETARY PROPERTIES

4.1. EXOFAST Global Fit

To perform a global fit of our photometric and spectroscopic data, we use a modified version of the IDL exoplanet fitting tool, EXOFAST (Eastman et al. 2013). More detailed explanation of the global modeling is provided in Siverd et al. (2012). To determine a system’s final parameters, simultaneous Markov Chain Monte Carlo (MCMC) analysis is performed on the AAT radial velocity measurements and the follow-up photometric observations. To constrain M_* and R_* EXOFAST uses either the Yonsei-Yale stellar evolution models (Demarque et al. 2004) or the empirical Torres relations (Torres et al. 2010). Each photometric observation’s raw light curve and the detrending parameters determined from

the light curve are inputs for the final fit. We impose a prior on T_{eff} and $[\text{Fe}/\text{H}]$ using the determined values and errors from the SME analysis of the AAT spectra. From analysis of the KELT-South and follow-up photometric observations, we set a prior on the period. For both KELT-14b and KELT-15b, we perform four global fits: 1) Using the Yonsei-Yale (YY) stellar models with eccentricity fixed at zero. We adopt the system parameters from this global fit for all analysis and interpretation for KELT-14b and KELT-15b. 2) Using the YY stellar models with eccentricity as a free parameter. 3) Using the empirical Torres relations with eccentricity fixed at zero. 4) Using the empirical Torres relations with eccentricity as a free parameter. The results from these four global fits can be seen in Table 6 for the KELT-14 system and Table 7 for the KELT-15 system. All determined values for the four separate global fits are consistent with each (within 1σ). We adopt the YY circular fit parameters for each system.

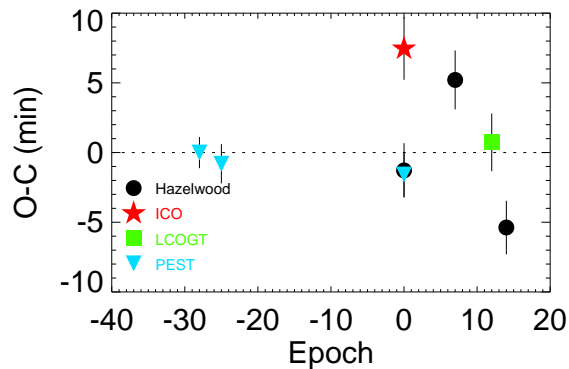


FIG. 9.— Transit time residuals for KELT-14b using our final global fit ephemeris. The times are listed in Table 8.

4.2. Transit Timing Variation Analysis

Using only the transit timing data shown in Table 8 and Figure 9, we determined a separate ephemeris from our global fit for KELT-14b. We were careful to confirm all observation times are in the BJD_TDB format (Eastman et al. 2010). To determine an independent ephemeris, we performed a linear fit to the transit center times inferred from the global fit for each follow-up observation. With a χ^2 of 26.9 and 6 degrees of freedom, we get $T_0 = 2457091.028632 \pm 0.00046884453$ (BJD_{TDB}) and a period of 1.7100588 ± 0.00000247 days. The high χ^2 is likely caused by systematics in the follow-up photometric observations. Therefore, we are unwilling to claim convincing evidence for transit timing variations for KELT-14b. With only three transits of KELT-15b, we do not attempt a TTV analysis.

5. FALSE POSITIVE ANALYSIS

A similar signal to a true planetary event can be created by a variety of astrophysical and non-astrophysical scenarios. All spectroscopic observations of both KELT-14 and KELT-15 were thoroughly analyzed to ensure that the observed signal was from the target star. There are no signs of multiple sets of absorption lines. As mentioned in §2.3.2, we find no correlation between the bisector spans and the measured radial velocities (see Figure 6). All transit depths across optical band passes are consistent and the global fit $\log g_*$ is consistent with the spectroscopic analysis for KELT-14. There

is some discrepancy in the KELT-15 $\log g_*$ from the global fit and SME analysis but this is because the AAT spectra do not include the gravity sensitive MgB triplet to provide a better constraint on $\log g_*$. Overall, we find no evidence that KELT-14b and KELT-15b are anything other than transiting exoplanets, but a better estimate of the $\log g_*$ of KELT-15 using a high-resolution spectrum covering the gravity sensitive MgB triplet would help confirm the planetary nature of the companion.

6. DISCUSSION

6.1. Evolution

As can be seen from the results of the global fit (Table 6 and 7), KELT-14b and KELT-15b are highly inflated planets, joining the ranks of other hot Jupiters that manifest radii much larger than predicted by standard, non-irradiated models. Several authors (e.g., Demory & Seager 2011) have suggested an empirical insolation threshold ($\approx 2 \times 10^8 \text{ erg s}^{-1} \text{ cm}^{-2}$) above which hot Jupiters exhibit increasing amounts of radius inflation. KELT-14b and KELT-15b clearly lie above this threshold, with a current estimated insolation of $2.98^{+0.36}_{-0.33} \times 10^9 \text{ erg s}^{-1} \text{ cm}^{-2}$ and $1.652^{+0.19}_{-0.100} \times 10^9 \text{ erg s}^{-1} \text{ cm}^{-2}$, respectively, from the global fits, and therefore their currently large inflated radii are not surprising. At the same time, the KELT-14 and KELT-15 host stars are both found to be at present in a state of evolution wherein the stellar radii are expanding as the stars prepare to cross the Hertzsprung gap toward the red giant branch. This means that the stars' surfaces are encroaching on their planets, which presumably is in turn driving up the planets' insulations and also the rate of any tidal interactions between the planets and the stars.

Therefore it is interesting to consider two questions. First, has KELT-14b's and KELT-15b's incident radiation from their host stars been below the empirical radius inflation threshold in the past? If either planet's insolation only recently exceeded the inflation threshold, the system could then serve as an empirical test bed for the different timescales predicted by different inflation mechanisms (see, e.g., Assef et al. 2009; Spiegel & Madhusudhan 2012). Second, what is the expected fate of the KELT-14b and KELT-15b planets given the increasingly strong tidal interactions they are experiencing with their encroaching host stars?

To investigate these questions, we follow Penev et al. (2014) to simulate the reverse and forward evolution of the star-planet system, using the measured parameters listed in Table 6 and 7 as the present-day boundary conditions. This analysis is not intended to examine any type of planet-planet or planet-disk migration effects. Rather, it is a way to investigate (1) the change in insolation of the planet over time due to the changing luminosity of the star and changing star-planet separation, and (2) the change in the planet's orbital semi-major axis due to the changing tidal torque as the star-planet separation changes with the evolving stellar radius. We include the evolution of the star, assumed to follow the Yonsei-Yale stellar model with mass and metallicity. For simplicity we assume that the stellar rotation is negligible and treat the star as a solid body. We also assume a circular orbit aligned with the stellar equator throughout the analysis. The results of our simulations are shown in Figure 10. We tested a range of values for the tidal quality factor of the star divided by the love number, $Q'_* \equiv Q_*/k_2$, from $\log Q'_* = 5$ to $\log Q'_* = 7$ (assuming a constant phase lag between the tidal bulge and the star-planet direction).

TABLE 6
 MEDIAN VALUES AND 68% CONFIDENCE INTERVAL FOR THE PHYSICAL AND ORBITAL PARAMETERS OF THE KELT-14 SYSTEM

Parameter	Units	Adopted Value (YY circular)	Value (YY eccentric)	Value (Torres circular)	Value (Torres eccentric)
Stellar Parameters					
M_*	Mass (M_\odot)	$1.178^{+0.052}_{-0.066}$	$1.177^{+0.059}_{-0.066}$	$1.202^{+0.064}_{-0.062}$	$1.203^{+0.066}_{-0.063}$
R_*	Radius (R_\odot)	$1.368^{+0.078}_{-0.077}$	$1.378^{+0.10}_{-0.099}$	1.410 ± 0.077	$1.418^{+0.096}_{-0.094}$
L_*	Luminosity (L_\odot)	$1.90^{+0.28}_{-0.24}$	$1.93^{+0.34}_{-0.29}$	$2.04^{+0.29}_{-0.26}$	$2.06^{+0.34}_{-0.30}$
ρ_*	Density (cgs)	$0.645^{+0.11}_{-0.087}$	$0.63^{+0.14}_{-0.11}$	$0.604^{+0.096}_{-0.078}$	$0.595^{+0.12}_{-0.094}$
$\log g_*$	Surface gravity (cgs)	$4.234^{+0.045}_{-0.041}$	$4.228^{+0.057}_{-0.054}$	$4.219^{+0.041}_{-0.038}$	$4.215^{+0.051}_{-0.048}$
T_{eff}	Effective temperature (K)	5802^{+95}_{-92}	5800^{+96}_{-92}	5815 ± 88	5815 ± 89
[Fe/H]	Metallicity	$0.326^{+0.091}_{-0.089}$	$0.324^{+0.092}_{-0.089}$	$0.338^{+0.087}_{-0.085}$	$0.338^{+0.086}_{-0.085}$
Planet Parameters					
e	Eccentricity	—	$0.041^{+0.036}_{-0.027}$	—	$0.039^{+0.034}_{-0.026}$
ω_*	Argument of periastron (degrees)	—	149^{+7}_{-65}	—	156^{+73}_{-69}
P	Period (days)	$1.7100596^{+0.0000074}_{-0.0000075}$	1.7100597 ± 0.0000074	$1.7100596^{+0.0000074}_{-0.0000073}$	1.7100596 ± 0.0000074
a	Semi-major axis (AU)	$0.02956^{+0.00043}_{-0.00057}$	$0.02955^{+0.00048}_{-0.00057}$	0.02976 ± 0.00052	0.02977 ± 0.00053
M_P	Mass (M_J)	1.196 ± 0.072	$1.206^{+0.079}_{-0.076}$	$1.217^{+0.075}_{-0.073}$	$1.226^{+0.081}_{-0.078}$
R_P	Radius (R_J)	$1.52^{+0.12}_{-0.11}$	1.53 ± 0.14	$1.57^{+0.12}_{-0.11}$	$1.57^{+0.14}_{-0.13}$
ρ_P	Density (cgs)	$0.421^{+0.11}_{-0.083}$	$0.414^{+0.12}_{-0.091}$	$0.393^{+0.095}_{-0.076}$	$0.390^{+0.11}_{-0.082}$
$\log g_P$	Surface gravity	$3.107^{+0.066}_{-0.064}$	$3.103^{+0.075}_{-0.071}$	3.089 ± 0.062	$3.088^{+0.068}_{-0.067}$
T_{eq}	Equilibrium temperature (K)	1904 ± 54	1910^{+68}_{-67}	1929^{+55}_{-56}	1934 ± 65
$\langle F \rangle$	Incident flux ($10^9 \text{ erg s}^{-1} \text{ cm}^{-2}$)	$2.98^{+0.36}_{-0.33}$	$3.02^{+0.45}_{-0.40}$	$3.15^{+0.38}_{-0.35}$	$3.17^{+0.45}_{-0.41}$
RV Parameters					
T_C	Time of inferior conjunction (BJD _{TDB})	2457111.5484 ± 0.0050	2457111.5497 ± 0.0052	$2457111.5485^{+0.0049}_{-0.0050}$	2457111.5496 ± 0.0051
T_P	Time of periastron (BJD _{TDB})	—	$2457111.81^{+0.36}_{-0.29}$	—	$2457111.84^{+0.35}_{-0.31}$
K	RV semi-amplitude (m/s)	179.8 ± 9.0	181.3 ± 9.3	179.7 ± 8.9	181.2 ± 9.2
$M_P \sin i$	Minimum mass (M_J)	$1.177^{+0.071}_{-0.070}$	$1.185^{+0.076}_{-0.074}$	$1.196^{+0.073}_{-0.072} \& 1.204^{+0.078}_{-0.075}$	—
M_P/M_*	Mass ratio	$0.000974^{+0.000052}_{-0.000051}$	$0.000981^{+0.000053}_{-0.000052}$	$0.000967^{+0.000051}_{-0.000050}$	0.000973 ± 0.000052
u	RM linear limb darkening	0.668 ± 0.011	0.668 ± 0.011	0.668 ± 0.011	0.668 ± 0.011
γ_{AAT}	m/s	$34590.0^{+6.8}_{-6.7}$	34590.3 ± 6.7	34590.0 ± 6.7	34590.3 ± 6.6
$\dot{\gamma}$	RV slope (m/s/day)	0.53 ± 0.20	0.52 ± 0.23	0.52 ± 0.20	0.53 ± 0.22
$e \cos \omega_*$		—	$-0.019^{+0.021}_{-0.028}$	—	$-0.018^{+0.020}_{-0.028}$
$e \sin \omega_*$		—	$0.005^{+0.045}_{-0.033}$	—	$0.003^{+0.040}_{-0.032}$
Primary Transit					
R_P/R_*	Radius of the planet in stellar radii	$0.1143^{+0.0029}_{-0.0026}$	$0.1142^{+0.0029}_{-0.0026}$	$0.1141^{+0.0029}_{-0.0026}$	$0.1141^{+0.0030}_{-0.0026}$
a/R_*	Semi-major axis in stellar radii	$4.64^{+0.25}_{-0.22}$	$4.60^{+0.25}_{-0.28}$	$4.54^{+0.23}_{-0.20}$	$4.51^{+0.28}_{-0.25}$
i	Inclination (degrees)	$79.67^{+0.80}_{-0.77}$	79.5 ± 1.2	79.36 ± 0.75	79.2 ± 1.1
b	Impact parameter	$0.831^{+0.020}_{-0.022}$	$0.831^{+0.020}_{-0.022}$	$0.838^{+0.018}_{-0.020}$	$0.837^{+0.019}_{-0.021}$
δ	Transit depth	$0.01306^{+0.00067}_{-0.00059}$	$0.01305^{+0.00067}_{-0.00059}$	$0.01302^{+0.00067}_{-0.00058}$	$0.01301^{+0.00068}_{-0.00058}$
T_O	Ephemeris from transits (BJD _{TDB})	$2457091.028632 \pm 0.00047$	—	—	—
P_{Transits}	Ephemeris period from transits (days)	1.7100588 ± 0.000025	—	—	—
T_{FWHM}	FWHM duration (days)	$0.0626^{+0.0018}_{-0.0025}$	$0.0626^{+0.0017}_{-0.0025}$	$0.0625^{+0.0019}_{-0.0028}$	$0.0625^{+0.0019}_{-0.0028}$
τ	Ingress/egress duration (days)	$0.0262^{+0.0046}_{-0.0037}$	$0.0261^{+0.0046}_{-0.0036}$	$0.0274^{+0.0048}_{-0.0037}$	$0.0274^{+0.0049}_{-0.0037}$
T_{14}	Total duration (days)	$0.0889^{+0.0025}_{-0.0026}$	0.0888 ± 0.0026	$0.0900^{+0.0024}_{-0.0025}$	0.0900 ± 0.0025
P_T	A priori non-grazing transit probability	$0.1910^{+0.0089}_{-0.0094}$	$0.194^{+0.020}_{-0.017}$	$0.1952^{+0.0086}_{-0.0089}$	$0.197^{+0.018}_{-0.016}$
$P_{T,G}$	A priori transit probability	$0.240^{+0.012}_{-0.013}$	$0.244^{+0.025}_{-0.022}$	0.246 ± 0.012	$0.248^{+0.023}_{-0.021}$
u_{1B}	Linear Limb-darkening	0.685 ± 0.026	$0.685^{+0.027}_{-0.026}$	$0.684^{+0.026}_{-0.025}$	$0.684^{+0.026}_{-0.025}$
u_{2B}	Quadratic Limb-darkening	$0.134^{+0.020}_{-0.021}$	$0.133^{+0.020}_{-0.021}$	0.135 ± 0.020	0.135 ± 0.020
u_{1I}	Linear Limb-darkening	$0.294^{+0.015}_{-0.014}$	0.294 ± 0.015	0.293 ± 0.014	0.292 ± 0.014
u_{2I}	Quadratic Limb-darkening	$0.2810^{+0.0074}_{-0.0075}$	0.2810 ± 0.0075	$0.2824^{+0.0070}_{-0.0072}$	$0.2825^{+0.0071}_{-0.0073}$
u_{1R}	Linear Limb-darkening	$0.382^{+0.018}_{-0.017}$	0.382 ± 0.018	$0.380^{+0.018}_{-0.017}$	$0.380^{+0.018}_{-0.017}$
u_{2R}	Quadratic Limb-darkening	$0.2777^{+0.0096}_{-0.010}$	$0.2776^{+0.0098}_{-0.010}$	$0.2789^{+0.0094}_{-0.0098}$	$0.2790^{+0.0093}_{-0.0099}$
$u_{1Sloang}$	Linear Limb-darkening	$0.602^{+0.025}_{-0.024}$	$0.602^{+0.026}_{-0.025}$	$0.601^{+0.025}_{-0.024}$	$0.601^{+0.025}_{-0.024}$
$u_{2Sloang}$	Quadratic Limb-darkening	$0.188^{+0.017}_{-0.018}$	$0.188^{+0.018}_{-0.019}$	$0.189^{+0.017}_{-0.018}$	$0.189^{+0.017}_{-0.018}$
u_{1V}	Linear Limb-darkening	0.484 ± 0.021	$0.484^{+0.022}_{-0.021}$	$0.483^{+0.021}_{-0.020}$	$0.483^{+0.021}_{-0.020}$
u_{2V}	Quadratic Limb-darkening	$0.247^{+0.013}_{-0.014}$	$0.247^{+0.013}_{-0.014}$	0.248 ± 0.013	$0.248^{+0.013}_{-0.014}$
Secondary Eclipse					
T_S	Time of eclipse (BJD _{TDB})	2457110.6934 ± 0.0050	$2457112.384^{+0.022}_{-0.029}$	$2457110.6935^{+0.0049}_{-0.0050}$	$2457112.384^{+0.022}_{-0.029}$
b_S	Impact parameter	—	$0.842^{+0.080}_{-0.063}$	—	$0.845^{+0.071}_{-0.059}$
$T_{S,FWHM}$	FWHM duration (days)	—	$0.0609^{+0.0065}_{-0.019}$	—	$0.0612^{+0.0069}_{-0.019}$
τ_S	Ingress/egress duration (days)	—	$0.0275^{+0.013}_{-0.0071}$	—	$0.0286^{+0.013}_{-0.0071}$
$T_{S,14}$	Total duration (days)	—	$0.0872^{+0.0035}_{-0.0048}$	—	$0.0887^{+0.0034}_{-0.0045}$
P_S	A priori non-grazing eclipse probability	—	$0.1910^{+0.0091}_{-0.0094}$	—	$0.1953^{+0.0088}_{-0.0090}$
$P_{S,G}$	A priori eclipse probability	—	0.240 ± 0.013	—	0.246 ± 0.012

TABLE 7
 MEDIAN VALUES AND 68% CONFIDENCE INTERVAL FOR THE PHYSICAL AND ORBITAL PARAMETERS OF THE KELT-15 SYSTEM

Parameter	Units	Preferred Value (YY circular)	Value (YY eccentric)	Value (Torres circular)	Value (Torres eccentric)
Stellar Parameters					
M_*	Mass (M_\odot)	$1.181^{+0.051}_{-0.050}$	$1.218^{+0.10}_{-0.071}$	$1.216^{+0.057}_{-0.055}$	$1.244^{+0.092}_{-0.074}$
R_*	Radius (R_\odot)	$1.481^{+0.091}_{-0.041}$	$1.63^{+0.30}_{-0.18}$	$1.493^{+0.082}_{-0.042}$	$1.60^{+0.34}_{-0.17}$
L_*	Luminosity (L_\odot)	$2.58^{+0.35}_{-0.20}$	$3.11^{+1.3}_{-0.69}$	$2.65^{+0.32}_{-0.20}$	$3.04^{+1.4}_{-0.65}$
ρ_*	Density (cgs)	$0.514^{+0.034}_{-0.076}$	$0.40^{+0.15}_{-0.14}$	$0.518^{+0.032}_{-0.071}$	$0.42^{+0.15}_{-0.17}$
$\log g_*$	Surface gravity (cgs)	$4.168^{+0.019}_{-0.044}$	$4.100^{+0.086}_{-0.11}$	$4.174^{+0.018}_{-0.040}$	$4.120^{+0.084}_{-0.14}$
T_{eff}	Effective temperature (K)	6003^{+56}_{-52}	6017^{+58}_{-57}	6021^{+60}_{-61}	6021^{+61}_{-60}
[Fe/H]	Metallicity	0.047 ± 0.032	$0.051^{+0.033}_{-0.032}$	$0.051^{+0.034}_{-0.033}$	0.051 ± 0.033
Planet Parameters					
e	Eccentricity	—	$0.132^{+0.13}_{-0.090}$	—	$0.133^{+0.14}_{-0.091}$
ω_*	Argument of periastron (degrees)	—	141^{+71}_{-42}	—	142^{+76}_{-42}
P	Period (days)	3.329441 ± 0.000016	3.329442 ± 0.000016	3.329441 ± 0.000016	3.329442 ± 0.000016
a	Semi-major axis (AU)	0.04613 ± 0.00065	$0.04660^{+0.0013}_{-0.00092}$	0.04657 ± 0.00072	$0.04693^{+0.0011}_{-0.00095}$
M_P	Mass (M_J)	$0.91^{+0.21}_{-0.22}$	$0.94^{+0.26}_{-0.25}$	0.93 ± 0.22	$0.95^{+0.26}_{-0.25}$
R_P	Radius (R_J)	$1.443^{+0.11}_{-0.057}$	$1.59^{+0.31}_{-0.19}$	$1.453^{+0.098}_{-0.057}$	$1.56^{+0.34}_{-0.18}$
ρ_P	Density (cgs)	$0.36^{+0.11}_{-0.10}$	$0.28^{+0.15}_{-0.11}$	$0.363^{+0.11}_{-0.100}$	$0.29^{+0.16}_{-0.13}$
$\log g_P$	Surface gravity	$3.02^{+0.10}_{-0.13}$	$2.95^{+0.14}_{-0.17}$	$3.03^{+0.10}_{-0.12}$	$2.96^{+0.15}_{-0.18}$
T_{eq}	Equilibrium temperature (K)	1642^{+45}_{-25}	1713^{+140}_{-92}	1645^{+140}_{-25}	1699^{+150}_{-87}
$\langle F \rangle$	Incident flux ($10^9 \text{ erg s}^{-1} \text{ cm}^{-2}$)	$1.652^{+0.19}_{-0.100}$	$1.92^{+0.58}_{-0.37}$	$1.66^{+0.17}_{-0.10}$	$1.86^{+0.63}_{-0.35}$
RV Parameters					
T_C	Time of inferior conjunction (BJD _{TDB})	$2457029.1663^{+0.0078}_{-0.0073}$	$2457029.1691^{+0.0083}_{-0.0081}$	$2457029.1663^{+0.0079}_{-0.0073}$	$2457029.1688^{+0.0084}_{-0.0080}$
T_P	Time of periastron (BJD _{TDB})	—	$2457029.49^{+0.64}_{-0.29}$	—	$2457029.50^{+0.71}_{-0.29}$
K	RV semi-amplitude (m/s)	110 ± 26	113 ± 30	110 ± 26	113^{+30}_{-29}
$M_P \sin i$	Minimum mass (M_J)	$0.91^{+0.21}_{-0.22}$	$0.94^{+0.26}_{-0.25}$	0.93 ± 0.22	$0.95^{+0.26}_{-0.25}$
M_P/M_*	Mass ratio	0.00073 ± 0.00017	0.00073 ± 0.00019	0.00073 ± 0.00017	0.00073 ± 0.00019
u	RM linear limb darkening	$0.6290^{+0.0062}_{-0.0058}$	$0.6275^{+0.0065}_{-0.0059}$	$0.6276^{+0.0066}_{-0.0060}$	$0.6272^{+0.0066}_{-0.0060}$
γ_{AAT}	m/s	12204^{+18}_{-19}	12203 ± 21	12204 ± 19	12204 ± 20
γ_{CORALIE}	m/s	12216 ± 22	12212 ± 22	12216 ± 21	12211 ± 22
$e \cos \omega_*$		—	$-0.073^{+0.073}_{-0.10}$	—	$-0.074^{+0.074}_{-0.10}$
$e \sin \omega_*$		—	$0.050^{+0.14}_{-0.082}$	—	$0.042^{+0.16}_{-0.085}$
Primary Transit					
R_P/R_*	Radius of the planet in stellar radii	$0.1001^{+0.0022}_{-0.0021}$	$0.1005^{+0.0025}_{-0.0023}$	$0.1001^{+0.0021}_{-0.0020}$	$0.1001^{+0.0022}_{-0.0021}$
a/R_*	Semi-major axis in stellar radii	$6.70^{+0.14}_{-0.35}$	$6.16^{+0.68}_{-0.83}$	$6.72^{+0.13}_{-0.32}$	$6.29^{+0.67}_{-0.99}$
i	Inclination (degrees)	$88.3^{+1.2}_{-1.7}$	$87.8^{+1.6}_{-2.3}$	$88.4^{+1.1}_{-1.6}$	$88.1^{+1.3}_{-1.5}$
b	Impact parameter	$0.20^{+0.18}_{-0.14}$	$0.22^{+0.19}_{-0.15}$	$0.19^{+0.17}_{-0.13}$	$0.20^{+0.17}_{-0.13}$
δ	Transit depth	$0.01003^{+0.00044}_{-0.00041}$	$0.01009^{+0.00050}_{-0.00046}$	$0.01001^{+0.00043}_{-0.00040}$	$0.01002^{+0.00044}_{-0.00041}$
T_{FWHM}	FWHM duration (days)	$0.1552^{+0.0015}_{-0.0016}$	$0.1552^{+0.0017}_{-0.0018}$	$0.1551^{+0.0015}_{-0.0016}$	0.1550 ± 0.0016
τ	Ingress/egress duration (days)	$0.01635^{+0.00021}_{-0.00070}$	$0.01656^{+0.00026}_{-0.00093}$	$0.01627^{+0.00019}_{-0.00074}$	$0.01631^{+0.00020}_{-0.00076}$
T_{14}	Total duration (days)	$0.1719^{+0.0025}_{-0.0021}$	$0.1722^{+0.0030}_{-0.0024}$	$0.1717^{+0.0024}_{-0.0021}$	$0.1717^{+0.0025}_{-0.0021}$
P_T	A priori non-grazing transit probability	$0.1343^{+0.0072}_{-0.0027}$	$0.155^{+0.058}_{-0.026}$	$0.1340^{+0.0066}_{-0.0026}$	$0.151^{+0.068}_{-0.025}$
$P_{T,G}$	A priori transit probability	$0.1642^{+0.0092}_{-0.0036}$	$0.190^{+0.070}_{-0.032}$	$0.1637^{+0.0084}_{-0.0033}$	$0.185^{+0.084}_{-0.031}$
u_{1l}	Linear Limb-darkening	$0.2500^{+0.0078}_{-0.0069}$	$0.2471^{+0.0086}_{-0.0079}$	$0.2482^{+0.0083}_{-0.0073}$	$0.2468^{+0.0086}_{-0.0077}$
u_{2l}	Quadratic Limb-darkening	$0.2964^{+0.0027}_{-0.0036}$	$0.2980^{+0.0036}_{-0.0040}$	$0.2972^{+0.0028}_{-0.0037}$	$0.2980^{+0.0034}_{-0.0039}$
u_{1R}	Linear Limb-darkening	$0.3259^{+0.0092}_{-0.0080}$	$0.3231^{+0.0098}_{-0.0086}$	$0.3237^{+0.0098}_{-0.0083}$	$0.3227^{+0.0098}_{-0.0085}$
u_{2R}	Quadratic Limb-darkening	$0.3027^{+0.0033}_{-0.0046}$	$0.3042^{+0.0038}_{-0.0048}$	$0.3037^{+0.0035}_{-0.0048}$	$0.3043^{+0.0037}_{-0.0048}$
u_{1V}	Linear Limb-darkening	$0.4158^{+0.011}_{-0.0091}$	$0.4132^{+0.011}_{-0.0092}$	$0.4133^{+0.011}_{-0.0094}$	$0.4127^{+0.011}_{-0.0094}$
u_{2V}	Quadratic Limb-darkening	$0.2858^{+0.0045}_{-0.0061}$	$0.2871^{+0.0044}_{-0.0061}$	$0.2871^{+0.0046}_{-0.0062}$	$0.2874^{+0.0045}_{-0.0061}$
Secondary Eclipse					
T_S	Time of eclipse (BJD _{TDB})	$2457027.5016^{+0.0078}_{-0.0073}$	$2457030.68^{+0.16}_{-0.22}$	$2457027.5015^{+0.0079}_{-0.0073}$	$2457030.68^{+0.16}_{-0.22}$
b_S	Impact parameter	—	$0.25^{+0.22}_{-0.17}$	—	$0.22^{+0.22}_{-0.15}$
$T_{S,FWHM}$	FWHM duration (days)	—	$0.168^{+0.046}_{-0.022}$	—	$0.166^{+0.052}_{-0.024}$
τ_S	Ingress/egress duration (days)	—	$0.0193^{+0.0076}_{-0.0039}$	—	$0.0185^{+0.0085}_{-0.0036}$
$T_{S,14}$	Total duration (days)	—	$0.189^{+0.026}_{-0.026}$	—	$0.186^{+0.028}_{-0.028}$
P_S	A priori non-grazing eclipse probability	—	$0.1394^{+0.011}_{-0.0057}$	—	$0.1383^{+0.011}_{-0.0051}$
$P_{S,G}$	A priori eclipse probability	—	$0.1705^{+0.014}_{-0.0072}$	—	$0.1690^{+0.014}_{-0.0064}$

TABLE 8
TRANSIT TIMES FOR KELT-14b.

Epoch	T_C (BJD _{TDB})	σ_{T_C} (s)	O-C (s)	O-C (σ_{T_C})	Telescope
-29	2457043.146899	67	-5.00	-0.07	PEST
-26	2457048.276707	83	-37.99	-0.45	PEST
-1	2457091.027548	93	-102.01	-1.09	PEST
-1	2457091.033997	134	455.19	3.37	ICO
-1	2457091.027674	121	-91.12	-0.75	Hazelwood
6	2457103.002776	119	311.42	2.60	Hazelwood
11	2457111.550157	169	57.80	0.34	LCOGT
13	2457114.965950	113	-316.62	-2.78	Hazelwood

We find that although for certain values of Q'_* the planets may have been initially below the insolation inflation threshold during the first ~ 100 Myr, in all cases the planets have always received more than enough flux from their hosts to keep the planets irradiated beyond the insolation threshold identified by Demory & Seager (2011).

KELT-15b appears destined to survive for at least the next few Gyr, unless the stellar Q'_* is very small, in which case it is predicted to experience a rapid in-spiral into its host star. In the case of KELT-14b, the current evolution of the star suggests a concomitant in-spiral of the planet over the next ~ 1 Gyr, and even faster if the stellar Q'_* is small. This planet therefore does not appear destined to survive beyond the star’s subgiant phase. As additional systems like KELT-14b are discovered and their evolution investigated in detail, it will be interesting to examine the statistics of planet survival and to compare these to predictions such as those shown here in Figure 10 to constrain mechanisms of planet-star interaction generally and the values of Q'_* specifically.

6.2. Opportunities for Atmospheric Characterization

Because of its very high equilibrium temperature (1904 K) and its bright K -band magnitude ($K = 9.424$), KELT-14b is an excellent target for detailed atmospheric characterization. Specifically we note that it is an especially ideal target for eclipse observations. Measurements during the secondary eclipse of a hot Jupiter provide a direct measurement of thermal emission from the planet’s dayside and allow constraints on the connection between the atmospheric structure and climate and irradiation from the host star. As illustrated in Figure 11, KELT-14b has the second largest expected emission signal in the K -band for known transiting planets brighter than $K < 10.5$. We therefore encourage follow up of this planet in eclipse in order to aid comparative studies of exoplanet atmospheres and better understand the connection between irradiation, albedo, and atmospheric circulation.

With an equilibrium temperature of 1642 K, KELT-15b is not as hot as KELT-14b. However, it still has a comparably large expected emission signal in the K band that should be detectable with ground-based telescopes. Observing multiple planets in eclipse that span a range of temperatures and other properties is particularly useful for comparative exoplanetology.

6.3. Spectroscopic Follow-up

From our global fit, we find that KELT-14b has a 0.53 ± 0.20 $\text{m s}^{-1} \text{day}^{-1}$ RV slope. It is possible that this RV trend is from a tertiary component in the system. Another discovery from the KELT survey, KELT-6b, showed a -0.239 ± 0.037 $\text{m s}^{-1} \text{day}^{-1}$ slope in the RV analysis (Collins et al. 2014). Recently, the RV slope of KELT-6 has been confirmed to be the result of

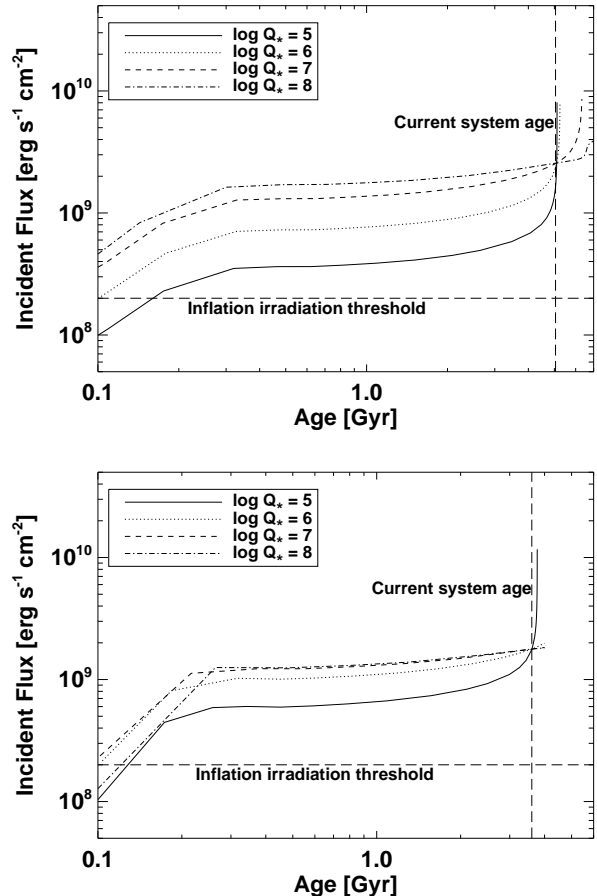


FIG. 10.— The inflation irradiation history for (top) KELT-14 and (bottom) KELT-15 shown for test values of $\log Q'_*$ of 5 to 8. The model assumes the stellar rotation is negligible and treats the star as a solid body. Also the model assumes a circular orbit aligned with the stellar equator. For both KELT-14b and KELT-15b, we find the insolation received is above the empirical threshold (horizontal dashed line) determined by Demory & Seager (2011). The vertical line represents the estimated current age of the system.

KELT-6c, a 3.5 year period companion with a minimum mass of $M_p \sin i = 3.71 \pm 0.21 M_J$ (Damasso et al. 2015). We therefore recommend long term spectroscopic follow-up of KELT-14 to try and characterize the long term trend we observed. Also, both KELT-14b and KELT-15b have Rossiter-McLaughlin (R-M) effects that can be detected with current ground-based facilities ($\sim 90 \text{ m s}^{-1}$). Two of our radial velocity observations of KELT-15b were taken during the transit and hint at a prograde orbit. However, due to our limited data acquired in transit, we do not claim KELT-15b to be in a prograde orbit but suggest future R–M observations to determine the spin-orbit alignment of the system.

7. SUMMARY AND CONCLUSIONS

We present the discovery of two more transiting inflated hot Jupiter exoplanets from the KELT-South survey, KELT-14b and KELT-15b. KELT-14b, the independent discovery of WASP-122b (Turner et al. 2015) has a period of $1.7100596^{+0.0000074}_{-0.0000075}$ days, a radius of $1.52^{+0.12}_{-0.11} R_J$ and a mass of $1.196 \pm 0.072 M_J$. KELT-15b has a period of 3.329441 ± 0.000016 days, a radius of $1.443^{+0.11}_{-0.057} R_J$ and a mass of $0.91^{+0.21}_{-0.22} M_J$. Additional follow-up transits are highly desirable for KELT-15b in order to better refine the ephemeris

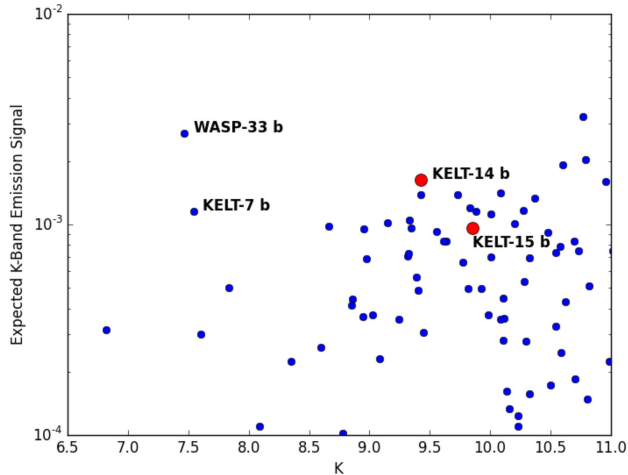


FIG. 11.— The expected emission signal in the K -band (assuming no redistribution of heat) for all known transiting planets brighter than a K -band magnitude of 11. Along with KELT-14b and KELT-15b, we highlight WASP-33b, one of the hottest known transiting planets and KELT-7b, another very hot and very bright planet discovered by the northern component of the KELT survey. Data are from this paper and the NASA Exoplanet Archive, accessed on 2015 August 27.

for future follow-up studies. Both KELT-14b and KELT-15b orbit host stars that are bright in the near-IR ($K = 9.424$ and 9.854 , respectively), making them attractive targets for atmospheric characterization through secondary eclipse observations. Both should have large enough emission signals that they can be observed using ground-based observatories.

These newly discovered planets increase the number of targets suitable for atmospheric characterization in the southern hemisphere.

ACKNOWLEDGEMENTS

KELT-South is hosted by the South African Astronomical Observatory and we are grateful for their ongoing support and assistance. K.P. acknowledges support from NASA grant NNX13AQ62G. Work by B.S.G. and D.J.S. was partially supported by NSF CAREER Grant AST-1056524. Work by K.G.S. was supported by NSF PAARE grant AST-1358862. D.W. and C.G.T.'s role in this research has been supported by ARC LIEF grant LE0989347, ARC Super Science Fellowship FS100100046, and ARC Discovery grant DP130102695.

This publication makes use of data products from the Wide-field Infrared Survey Explorer, which is a joint project of the University of California, Los Angeles, and the Jet Propulsion Laboratory/California Institute of Technology, funded by the National Aeronautics and Space Administration. This publication makes use of data products from the Two Micron All Sky Survey, which is a joint project of the University of Massachusetts and the Infrared Processing and Analysis Center/California Institute of Technology, funded by the National Aeronautics and Space Administration and the National Science Foundation.

This research was made possible through the use of the AAVSO Photometric All-Sky Survey (APASS), funded by the Robert Martin Ayers Sciences Fund. This paper uses observations obtained with facilities of the Las Cumbres Observatory Global Telescope.

REFERENCES

- , A. A., Levine, S., Terrell, D., & Welch, D. L. 2015, in American Astronomical Society Meeting Abstracts, Vol. 225, American Astronomical Society Meeting Abstracts, 336.16
- Addison, B. C., Tinney, C. G., Wright, D. J., & Bayliss, D. 2014, *ApJ*, 792, 112
- Addison, B. C., Tinney, C. G., Wright, D. J., et al. 2013, *ApJ*, 774, L9
- Alonso, R., Brown, T. M., Torres, G., et al. 2004, *ApJ*, 613, L153
- Ammons, S. M., Robinson, S. E., Strader, J., et al. 2006, *ApJ*, 638, 1004
- Assef, R. J., Gaudi, B. S., & Stanek, K. Z. 2009, *ApJ*, 701, 1616
- Baglin, A., Auvergne, M., Boissard, L., et al. 2006, in COSPAR Meeting, Vol. 36, 36th COSPAR Scientific Assembly, 3749
- Bakos, G., Noyes, R. W., Kovács, G., et al. 2004, *PASP*, 116, 266
- Baranne, A., Queloz, D., Mayor, M., et al. 1996, *A&AS*, 119, 373
- Bayliss, D., Zhou, G., Penev, K., et al. 2013, *AJ*, 146, 113
- Beatty, T. G., Pepper, J., Siverd, R. J., et al. 2012, *ApJ*, 756, L39
- Bensby, T., Feltzing, S., & Lundström, I. 2003, *A&A*, 410, 527
- Bieryla, A., Collins, K., Beatty, T. G., et al. 2015, *AJ*, 150, 12
- Borucki, W. J., Koch, D., Basri, G., et al. 2010, *Science*, 327, 977
- Castelli, F., & Kurucz, R. L. 2004, *ArXiv Astrophysics e-prints*, astro-ph/0405087
- Cloutier, R., & Lin, M.-K. 2013, *MNRAS*, 434, 621
- Collins, K., & Kielkopf, J. 2013, *AstroImageJ: ImageJ for Astronomy*, Astrophysics Source Code Library, ascl:1309.001
- Collins, K. A. 2015, High-precision time-series photometry for the discovery and characterization of transiting exoplanets., Electronic Theses and Dissertations, University of Louisville
- Collins, K. A., Eastman, J. D., Beatty, T. G., et al. 2014, *AJ*, 147, 39
- Cutri, R. M., & et al. 2012, *VizieR Online Data Catalog*, 2311, 0
- Cutri, R. M., Skrutskie, M. F., van Dyk, S., et al. 2003, *VizieR Online Data Catalog*, 2246, 0
- Damasso, M., Esposito, M., Nascimbeni, V., et al. 2015, *A&A*, 581, L6
- D'Angelo, G., & Lubow, S. H. 2008, *ApJ*, 685, 560
- Demarque, P., Woo, J.-H., Kim, Y.-C., & Yi, S. K. 2004, *ApJS*, 155, 667
- Demory, B.-O., & Seager, S. 2011, *ApJS*, 197, 12
- Dopita, M., Hart, J., McGregor, P., et al. 2007, *Ap&SS*, 310, 255
- Eastman, J., Gaudi, B. S., & Agol, E. 2013, *PASP*, 125, 83
- Eastman, J., Siverd, R., & Gaudi, B. S. 2010, *PASP*, 122, 935
- Fulton, B. J., Collins, K. A., Gaudi, B. S., et al. 2015, *ApJ*, 810, 30
- Gómez Maqueo Chew, Y., Faedi, F., Cargile, P., et al. 2013, *ApJ*, 768, 79
- Hartman, J. 2012, *VARTOOLS: Light Curve Analysis Program*, Astrophysics Source Code Library, ascl:1208.016
- Hög, E., Fabricius, C., Makarov, V. V., et al. 2000, *A&A*, 355, L27
- Horton, A., Tinney, C. G., Case, S., et al. 2012, in Society of Photo-Optical Instrumentation Engineers (SPIE) Conference Series, Vol. 8446, Society of Photo-Optical Instrumentation Engineers (SPIE) Conference Series, 3
- Hubeny, I., & Lanz, T. 2011, *Synspec: General Spectrum Synthesis Program*, Astrophysics Source Code Library, ascl:1109.022
- Jackson, B., Greenberg, R., & Barnes, R. 2008, *ApJ*, 678, 1396
- Jensen, E. 2013, *Tapir: A web interface for transits/eclipse observability*, Astrophysics Source Code Library, ascl:1306.007
- Kovács, G., Zucker, S., & Mazeh, T. 2002, *A&A*, 391, 369
- Kuhn, R. B., Rodriguez, J. E., Collins, K. A., et al. 2015, *ArXiv e-prints*, arXiv:1509.02323
- Martin, D. C., Fanson, J., Schiminovich, D., et al. 2005, *ApJ*, 619, L1
- Masset, F. S., & Papaloizou, J. C. B. 2003, *ApJ*, 588, 494
- McCullough, P. R., Stys, J. E., Valenti, J. A., et al. 2006, *ApJ*, 648, 1228
- Penev, K., Zhang, M., & Jackson, B. 2014, *PASP*, 126, 553
- Pepe, F., Mayor, M., Galland, F., et al. 2002, *A&A*, 388, 632
- Pepper, J., Kuhn, R. B., Siverd, R., James, D., & Stassun, K. 2012, *PASP*, 124, 230
- Pepper, J., Pogge, R. W., DePoy, D. L., et al. 2007, *PASP*, 119, 923
- Pepper, J., Siverd, R. J., Beatty, T. G., et al. 2013, *ApJ*, 773, 64
- Pickles, A., & Depagne, É. 2010, *PASP*, 122, 1437
- Pollacco, D. L., Skillen, I., Collier Cameron, A., et al. 2006, *PASP*, 118, 1407
- Queloz, D., Mayor, M., Udry, S., et al. 2001, *The Messenger*, 105, 1
- Schlegel, D. J., Finkbeiner, D. P., & Davis, M. 1998, *ApJ*, 500, 525
- Siverd, R. J., Beatty, T. G., Pepper, J., et al. 2012, *ApJ*, 761, 123
- Skrutskie, M. F., Cutri, R. M., Stiening, R., et al. 2006, *AJ*, 131, 1163
- Spiegel, D. S., & Madhusudhan, N. 2012, *ApJ*, 756, 132
- Tanaka, H., Takeuchi, T., & Ward, W. R. 2002, *ApJ*, 565, 1257
- Torres, G., Andersen, J., & Giménez, A. 2010, *A&A Rev.*, 18, 67
- Turner, O. D., Anderson, D. R., Collier Cameron, A., et al. 2015, *ArXiv e-prints*, arXiv:1509.02210

- Valenti, J. A., & Fischer, D. A. 2005, *ApJS*, 159, 141
- Valenti, J. A., & Piskunov, N. 1996, *A&AS*, 118, 595
- Walsh, K. J., Morbidelli, A., Raymond, S. N., O'Brien, D. P., & Mandell, A. M. 2011, *Nature*, 475, 206
- Wildi, F., Pepe, F., Chazelas, B., Lo Curto, G., & Lovis, C. 2011, in *Society of Photo-Optical Instrumentation Engineers (SPIE) Conference Series*, Vol. 8151, *Society of Photo-Optical Instrumentation Engineers (SPIE) Conference Series*, 1
- Wright, E. L., Eisenhardt, P. R. M., Mainzer, A. K., et al. 2010, *AJ*, 140, 1868
- Zacharias, N., Monet, D. G., Levine, S. E., et al. 2004, in *Bulletin of the American Astronomical Society*, Vol. 36, *American Astronomical Society Meeting Abstracts*, 1418